Feasibility and Operational Limits of a Low-Cost Indirect UAV Thermal Sensing System Based on Smartphone-Displayed Infrared Video

Yordan Stoyanov *, Atanasi Tashev, Silviya Salapateva, Penko Mitev, Dimitar Yankov, Galya Hristova, Galin Tihanov

Posted Date: 9 June 2026

doi: 10.20944/preprints202606.0679.v1

Keywords: UAV; thermal imaging; infrared camera; low-cost sensing; smartphone thermal camera; indirect thermal imaging; payload; motor temperature; battery endurance; display readability

 doi:10.20944/preprints202606.0679.v1

Article

Feasibility and Operational Limits of a Low-Cost Indirect UAV Thermal Sensing System Based on Smartphone-Displayed Infrared Video

Yordan Stoyanov [1,2,*], Atanasi Tashev [1], Silviya Salapateva [1], Penko Mitev [2,3], Dimitar Yankov [4], Galya Hristova [5] and Galin Tihanov [5]

[1] Technical University of Sofia, Branch Plovdiv, Department of Transport and Aircraft Equipment and Technologies, 25 Tsanko Dyustabanov str.,4000 Plovdiv, Bulgaria
[2] Center of competence "Smart mechatronic, eco-and energy-saving systems and technologies"
[3] Technical University of Sofia, Branch Plovdiv, Department of Mechanical and Instrument Engineering, 25 Tsanko Dyustabanov str.,4000 Plovdiv, Bulgaria
[4] Technical University of Sofia, Branch Plovdiv, Department of Electronics, 25 Tsanko Dyustabanov str.,4000 Plovdiv, Bulgaria
[5] Trakia University – Stara Zagora, Faculty of Agriculture, Department of Agricultural Engineering, Students campus, 6000, Bulgaria
* Correspondence: yordan.stoyanov@tu-plovdiv.bg

Highlights

What are the main findings?

- A low-cost indirect UAV thermal sensing workflow was experimentally evaluated using a DJI Mini 4K drone, a Servo King900 smartphone, and a UTi260M smartphone-connected thermal camera.
- The effective added payload was approximately 91 g, corresponding to 36.5% of the UAV mass, and reduced near-ground flight endurance by approximately 41.3%.

What are the implications of the main findings?

- The proposed system is feasible for short-range preliminary thermal screening, especially under nighttime or low-glare conditions.
- Payload mass, suspended-load oscillation, display readability, motor thermal loading, and lack of raw radiometric data are the main operational limits.

Abstract

Professional UAV thermal imaging systems are widely used for inspection, monitoring, and emergency applications, but their cost limits their use in educational, preliminary, and low-resource scenarios. This study evaluates a low-cost indirect UAV thermal sensing workflow based on a DJI Mini 4K consumer drone, a Servo King900 smartphone, and a UTi260M smartphone-connected infrared camera. The smartphone displayed and recorded the thermal stream, while the UAV onboard RGB camera recorded the smartphone-displayed infrared video during flight. The system was tested under no-payload and payload conditions, daylight and nighttime illumination, and several low-altitude operating heights. Motor temperatures were additionally inspected using a UTi260T thermal camera. The complete UAV–payload configuration had a measured mass of approximately 340 g, corresponding to an effective payload of 91 g and a payload-to-UAV mass ratio of 36.5%. Payload operation reduced flight endurance from approximately 25 min to 14 min 40 s and produced increased and asymmetric motor heating. Nighttime operation provided better display readability than daylight operation, with the best usability observed at approximately 5–15 m. The proposed workflow is feasible for short-range preliminary thermal screening, but it is limited by payload mass, suspended-load oscillation, display readability, endurance reduction, motor loading, and the absence of raw radiometric data.

 doi:10.20944/preprints202606.0679.v1

Keywords: UAV; thermal imaging; infrared camera; low-cost sensing; smartphone thermal camera; indirect thermal imaging; payload; motor temperature; battery endurance; display readability

1. Introduction

Unmanned aerial vehicles (UAVs) have become widely used platforms for visual inspection, environmental monitoring, infrastructure assessment, agricultural observation, search and rescue, wildlife monitoring, and remote sensing applications. Their ability to collect data from elevated positions, difficult-to-access locations, and hazardous environments makes them particularly useful for rapid field assessment. In addition to conventional RGB imaging, thermal imaging provides information that cannot be obtained from visible-light cameras alone, including surface temperature distribution, heat losses, thermal anomalies, warm objects, and human or animal presence under low-light or nighttime conditions.

Thermal UAV systems have been increasingly applied in wildlife monitoring, search and rescue, and environmental observation. Thermal infrared UAV data have been used for spatially explicit wildlife occupancy modelling [1], while drone-based thermal tracking has been investigated for search and rescue missions [2]. Thermal drones have also been applied for monitoring terrestrial mammals [3], improving wildlife detection through optimized flight-path design [4], and evaluating the influence of flight parameters on primate detection in tropical forests [5]. These studies show that thermal UAV performance depends not only on the thermal sensor, but also on target size, flight altitude, acquisition geometry, environmental contrast, and mission-planning strategy.

The operational limitations of thermal drones have also been highlighted in search and rescue and field-monitoring scenarios. Burke et al. reported that effective thermal drone use in marine and coastal search and rescue is constrained by target detectability, background conditions, mission geometry, and environmental factors [6]. Similar practical dependencies have been reported for nocturnal wildlife surveys, where sensor preparation, pre-programming, and operating conditions can influence detection performance [7]. These findings are relevant because they show that thermal UAV systems should be evaluated as complete operational workflows rather than as isolated sensor units.

Thermal UAV imaging is also widely used in technical, agricultural, and environmental inspection tasks. UAV-based thermal photogrammetry has been applied for agronomic information extraction using MATLAB-based processing workflows [8]. Thermal infrared cameras mounted on drones have been used for peat-fire detection and geolocation [9], urban surface heat monitoring [10], landfill monitoring [11], and mining exploration using UAVs, low-cost thermal cameras, and GIS tools [12]. UAV-based thermal imaging has also been used for agricultural object detection, such as stone detection on agricultural land [13], as well as for crop productivity and water-use assessment when combined with hyperspectral sensing [14]. These studies demonstrate the broad applicability of aerial thermal sensing, but they also show that reliable results depend strongly on flight conditions, data quality, processing workflow, and target-to-background thermal contrast.

In building and technical inspection, drone-based thermal approaches have been reviewed as promising tools for integrated building-envelope assessment [15], while UAV-mounted thermal cameras have been used for automatic detection of deteriorated photovoltaic modules [16]. In these applications, professional workflows typically rely on directly mounted thermal cameras, stabilized platforms, radiometric image acquisition, synchronized telemetry, flight planning, and post-processing tools. As a result, they can provide high-quality thermal data with known spatial, radiometric, and operational characteristics.

Recent developments in drone imaging and sensor-based situational awareness also show increasing interest in multimodal UAV sensing, real-time detection, and visible–thermal data integration [17–20]. These approaches are typically based on more advanced hardware and processing pipelines than the low-cost system investigated in the present work, but they provide

 doi:10.20944/preprints202606.0679.v1

useful context for understanding the role of sensor fusion, flight planning, coverage, and image-processing methods in UAV-based thermal applications.

Despite these advantages, professional UAV thermal platforms remain expensive and may be inaccessible for educational demonstrations, preliminary feasibility studies, rapid prototyping, and low-resource field screening. This creates practical interest in alternative low-cost configurations that can provide basic thermal information without attempting to replace professional radiometric UAV systems. Smartphone-compatible thermal cameras are one possible solution. These compact infrared modules can be connected to lightweight smartphones and can display or record thermal video through mobile applications. However, integrating such a system with a lightweight consumer UAV is not straightforward.

The main challenge is that lightweight consumer drones have limited payload capacity. Adding even a small smartphone–thermal camera module may significantly affect total mass, center of gravity, motor loading, battery endurance, flight stability, and safety margins. Furthermore, if the thermal information is displayed on a smartphone screen and then recorded indirectly by the onboard RGB camera of the UAV, the resulting data quality depends not only on the thermal camera but also on display brightness, ambient illumination, camera focus, display size in the frame, screen reflections, and suspended-load motion.

Therefore, such a configuration should not be considered equivalent to a professional UAV-mounted thermal camera. Instead, it should be treated as an indirect UAV thermal sensing workflow, where the primary thermal stream is generated by the smartphone-connected infrared camera, while the UAV RGB camera records the smartphone-displayed thermal information during flight. This creates a low-cost but technically limited approach that requires experimental validation.

More generally, experimental engineering studies in combustion analysis, machine vision, braking systems, thermo-structural analysis, and thermoelectric devices show that applied technical systems require careful evaluation of hardware configuration, operating conditions, sensor outputs, and model optimization [21–25]. Although these works address different engineering domains, they support the broader methodological view that experimental systems should be assessed together with their operational limits, measurement constraints, and optimization potential.

The present study evaluates a low-cost indirect UAV thermal sensing system based on a DJI Mini 4K consumer drone, a Servo King900 lightweight smartphone, and a UTi260M smartphone-connected infrared thermal camera. The smartphone–thermal camera module was suspended below the UAV using an ultralight cord-based mount, while the onboard RGB camera recorded the displayed thermal video stream during flight. Additional thermal inspections of the UAV motors were performed using a UTi260T handheld thermal camera in order to assess the influence of payload operation on propulsion system thermal loading.

The objective of this study is not to develop a professional radiometric UAV thermal imaging platform. Instead, the aim is to experimentally determine whether a minimal-cost UAV–smartphone–thermal camera configuration can provide usable thermal screening information under controlled low-altitude conditions and to identify its operational limits. The investigation focuses on payload mass, suspended-load stability, flight endurance, motor thermal loading, display readability, illumination conditions, operating height, warning occurrence, and the practical usability of the indirectly recorded thermal stream.

The main contributions of this study are as follows:

1. A low-cost indirect UAV thermal sensing workflow is proposed using a consumer drone, a lightweight smartphone, and a smartphone-connected LWIR thermal camera.
2. The payload mass and relative loading of the UAV platform are experimentally quantified.
3. The influence of the suspended smartphone–thermal camera module on flight endurance, stability, motor loading, and operational warnings is evaluated.
4. The readability of the smartphone-displayed thermal stream is compared under daylight and nighttime operating conditions.

 doi:10.20944/preprints202606.0679.v1

5. Direct thermal frames and UAV-recorded display frames are used to assess the practical usability and limitations of the proposed workflow.
6. The operational boundaries of the system are defined, including the effects of display glare, camera focus, payload oscillation, limited thermal resolution, motor thermal loading, and non-radiometric indirect acquisition.

The novelty of the work is not in proposing a professional UAV thermal imaging system, but in experimentally characterizing a low-cost, indirect, smartphone-based UAV thermal sensing configuration and its practical constraints. This includes the trade-off between payload mass, display readability, camera–display distance, suspended-load stability, motor thermal loading, flight endurance, and preliminary thermal target visibility.

2. Materials and Methods

2.1. Study Design and Experimental Workflow

This study was designed as an experimental feasibility and operational limits assessment of a low-cost indirect UAV thermal sensing workflow. The objective was to evaluate whether a lightweight consumer UAV could carry a smartphone-connected thermal camera module and whether the smartphone-displayed infrared video could be recorded by the UAV onboard RGB camera during flight.

The overall workflow included system assembly, payload characterization, flight testing, direct thermal frame acquisition, indirect UAV display recording, motor thermal inspection, image-based metric calculation, and operational limitation assessment. This structure follows the logic of sensor-based workflow reporting used in Sensors articles, where the data acquisition, processing, feature extraction, and interpretation pipeline is clearly shown before detailed measurements are presented.

The experimental UAV configuration and the general workflow used in the study are shown in Figure 1.

(**a**) (**b**)

Figure 1. Experimental system and workflow used in the study: (a) DJI Mini 4K during baseline no-payload operation; (b) DJI Mini 4K with the suspended Servo King900 smartphone and attached UTi260M thermal camera.

2.2. System Architecture and Sensor-Based Components

The experimental system consisted of a consumer UAV platform, a smartphone-connected thermal camera module, an auxiliary monitoring smartphone, and a handheld thermal camera for ground-based thermal inspection.

 doi:10.20944/preprints202606.0679.v1

The UAV platform was a DJI Mini 4K consumer drone. The airborne thermal module consisted of a Servo King900 lightweight smartphone connected to a UTi260M smartphone-compatible infrared thermal camera. The Servo King900 smartphone displayed and recorded the thermal video stream through the thermal camera application. During flight, the onboard RGB camera of the UAV recorded the smartphone-displayed thermal video stream. This created an indirect UAV-based thermal acquisition workflow.

A Ulefone Armor 27T smartphone was used for UAV control, monitoring, screen recording, and documentation. A UTi260T handheld thermal camera was used to inspect the UAV motor temperature distribution after selected no-payload and payload flights.

The system domains, components, data sources, measured parameters, and relevance to the proposed workflow are summarized in Table 1. This table is intentionally modeled after the system-domain table style used in the reference Sensors article, where hardware, sensing elements, measured parameters, and relevance are grouped in one compact methodological table.

The ground control and monitoring configuration used during the field tests is shown in Figure 2.

Figure 2. Ground control and monitoring configuration of the experimental UAV thermal sensing workflow. The DJI Mini 4K platform was operated using the remote controller and the Ulefone Armor 27T smartphone, which provided live UAV camera monitoring, telemetry visualization, and screen recording during the field tests.

Table 1. System domains, components, data sources, measured parameters, and relevance to the proposed indirect UAV thermal sensing workflow.

System domain	Component/feature	Data source	Measured/observed parameter	Relevance to the study
UAV platform	DJI Mini 4K	RGB video and telemetry overlay	Flight height, UAV motion, display visibility	Documents indirect acquisition and operating height
Thermal sensing	UTi260M	Smartphone application	Thermal images and video clips	Primary thermal stream

 doi:10.20944/preprints202606.0679.v1

Display and recording	Servo King900	Smartphone display/application	Smartphone-displayed thermal video	Enables indirect UAV recording of thermal information
Auxiliary monitoring	Ulefone Armor 27T	UAV control and screen recording	Flight monitoring and documentation	Supports experimental control
Ground thermal inspection	UTi260T	Still thermal images and PC software	Motor temperatures P1–P4	Evaluates payload-induced motor heating
Payload characterization	Digital scale	Mass measurements	UAV mass, payload mass, total mass	Quantifies payload ratio
Suspension geometry	Cord-based mount	Visual measurement	Camera–display distance, payload oscillation	Defines mechanical constraints
Image analysis	Exported frames	Grayscale conversion	Entropy, CV, SNR, contrast, UI	Relative image-information assessment

2.3. Payload Mass and Relative Loading

The masses of the UAV and payload components were measured using a digital scale. The bare DJI Mini 4K platform had a measured mass of approximately 249 g. The Servo King900 smartphone with the attached UTi260M thermal camera had a measured mass of approximately 95 g. The measured UAV mass and complete UAV–payload mass are shown in Figure 3.

The measured values are summarized in Table 2.

The effective added payload was calculated as:

$$m_{\text{payload}} = m_{total} - m_{\text{UAV}} \quad (1)$$

where m_{payload} is the effective payload mass, m_{total} is the measured mass of the complete UAV–payload configuration, and m_{UAV} is the measured mass of the UAV without the suspended module.

Using the measured values:

$$m_{\text{payload}} = 340 - 249 = 91g.$$

The relative payload ratio was calculated as:

$$PR = \frac{m_{\text{payload}}}{m_{\text{UAV}}} 100 \quad (2)$$

$$PR = \frac{91}{249} 100 = 36.5\%.$$

Thus, the effective payload represented approximately 36.5% of the UAV body mass. This is a substantial value for a lightweight consumer UAV platform and was expected to affect flight stability, motor loading, battery endurance, and operational safety margins.

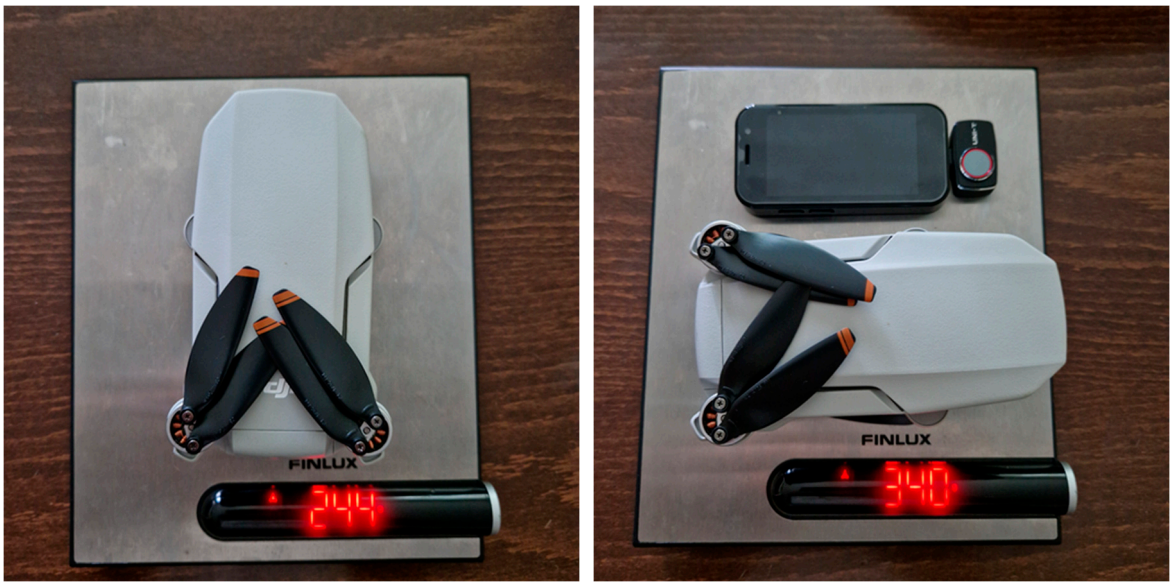

(**a**) (**b**)

Figure 3. *Payload characterization and suspension geometry of the experimental UAV thermal sensing configuration: (a) DJI Mini 4K platform mass; (b) Servo King900 smartphone with attached UTi260M thermal camera.*

 doi:10.20944/preprints202606.0679.v1

Table 2. Measured mass characteristics of the experimental UAV–payload configuration.

Parameter	Measured value
DJI Mini 4K mass	249 g
Servo King900 + UTi260M mass	95 g
Complete UAV–payload mass	340 g
Effective added payload	91 g
Payload-to-UAV mass ratio	36.5%

2.4. Payload Suspension and Camera–Display Geometry

The Servo King900 smartphone with the attached UTi260M thermal camera was suspended below the UAV using an ultralight cord-based mounting configuration. The approximate distance between the UAV onboard RGB camera and the smartphone display was 0.30 m, as shown in Figure 2.

This distance was selected as a practical compromise. At shorter distances, the smartphone display occupied a larger portion of the UAV camera frame, but the onboard RGB camera tended to lose focus. At longer distances, the display was easier to focus but became smaller in the recorded frame, reducing the readability of the displayed thermal stream. The selected 0.30 m configuration therefore represented a compromise between display size, focus, payload stability, and suspended-load oscillation.

However, the cord-based suspension introduced pendulum-like motion. This was particularly noticeable during take-off, vertical movement, hover correction, and small attitude adjustments. In addition, perfect alignment of the smartphone–thermal camera module with the UAV center of gravity was difficult to achieve.

Even a small horizontal offset between the payload center of mass and the UAV centerline could generate a destabilizing moment:

$$M = W_{payload} d,$$

where M is the moment caused by the suspended payload, $W_{payload}$ is the weight force of the smartphone–thermal camera module, and d is the horizontal offset from the UAV center of gravity.

The payload weight force was calculated as:

is the moment caused by the suspended payload, $W_{payload}$ is the weight force of the smartphone–thermal camera module, and d is the horizontal offset from the UAV center of gravity.

The payload weight force was calculated as:

$$W_{payload} = m_{payload} g,$$

where $g = 9.81\ m/s^2$. For the effective payload mass of 91 g:

$$W_{payload} = 0.091.9.81 = 0.0893\ N.$$

This force was not large in absolute terms, but its suspended position and possible offset from the UAV center of gravity created additional control demands for the propulsion system.

2.5. Experimental Flight Conditions

The experimental tests were performed under several operating conditions.

No-payload baseline flights were performed to document the normal behavior of the UAV platform without the suspended thermal module. Payload flights were performed with the Servo King900 + UTi260M module suspended below the UAV in order to evaluate lifting capability, stability, endurance, display readability, and operational warnings.

Daylight flights were used to evaluate the effect of sunlight, glare, and reflections on the readability of the smartphone-displayed thermal stream. Nighttime flights were performed to determine whether reduced ambient illumination improved display readability and indirect thermal usability. Representative daylight and nighttime UAV-recorded frames are presented in Figure 4.

 doi:10.20944/preprints202606.0679.v1

Tests were conducted at several low-altitude operating heights, including approximately 5–6 m, 10–12 m, 14–15 m, 20–23 m, and up to approximately 28–30 m. These height ranges were extracted from the UAV telemetry overlay visible in the recorded RGB frames.

Motor thermal inspection tests were performed using the UTi260T thermal camera after selected no-payload and payload flights. These tests are presented in Figure 6.

The flight endurance was evaluated for no-payload and payload configurations. The no-payload near-ground hover endurance was approximately 25 min, while the payload configuration achieved approximately 14 min 40 s under non-ideal stabilization conditions.

2.6. Thermal and RGB Data Acquisition

The UTi260M thermal camera produced the primary thermal stream. This stream was displayed and recorded on the Servo King900 smartphone. The UAV onboard RGB camera recorded the smartphone display during flight, producing a secondary video channel of the displayed thermal stream.

Therefore, two types of visual data were considered: direct thermal frames from the smartphone-connected UTi260M thermal camera and indirect UAV RGB frames showing the smartphone-displayed thermal video during flight.

The direct thermal frames were treated as the primary source for thermal interpretation and verification, while the UAV RGB recordings were treated as secondary evidence of the feasibility and limitations of indirect display-based acquisition. Representative examples of both channels are shown in Figures 4 and 5.

This distinction is important. The UAV RGB frames do not represent direct radiometric UAV thermal data. They show a smartphone display recorded by an RGB camera and are therefore affected by display brightness, camera focus, exposure, glare, screen reflections, compression, and suspended-load motion.

2.7. Thermal Data Format and Radiometric Limitations

The thermal data format represents an important methodological limitation of the proposed low-cost workflow. The UTi260M smartphone-connected thermal camera operates only through a dedicated mobile application. In the present configuration, the device was able to acquire thermal images and video clips through the smartphone application, but it did not provide direct access to raw radiometric matrices, sensor-level temperature arrays, or frame-by-frame radiometric export. Therefore, the UTi260M data used in this study were treated as application-level thermal images and videos rather than fully radiometric raw data.

The UTi260T handheld thermal camera was also used for thermal image and video acquisition. However, only still thermal images from the UTi260T could be further inspected and processed using the available PC software. Although video recording was possible, the thermal video files were not available as raw radiometric sequences for quantitative frame-by-frame processing. Consequently, the quantitative thermal assessment in this study was based on still thermal images, application-displayed temperature values, grayscale-converted thermal frames, and comparative image-based metrics rather than direct raw sensor matrices.

Because the internal radiometric processing and application-level thermal mapping algorithms of the UTi260M and UTi260T are proprietary and raw radiometric matrices were not exported, the analysis was based on application-level thermal frames and comparative image-based metrics. This is methodologically similar to how proprietary sensing systems are handled in some Sensors papers, where internal detection or processing rules are acknowledged as unavailable and exported data are used for analysis .

Entropy, contrast, standard deviation, coefficient of variation, and signal-to-noise ratio were calculated from exported thermal images or grayscale-converted thermal frames. These parameters were interpreted as relative indicators of image information content, contrast, and visual usability, not as absolute radiometric accuracy metrics. Similarly, motor temperature values obtained from the

 doi:10.20944/preprints202606.0679.v1

UTi260T software were used for comparative evaluation between payload and no-payload conditions, not as traceable laboratory-grade thermometric measurements.

2.8. Image Quality, Entropy, and Contrast Metrics

Image-based quality indicators were calculated to support the qualitative evaluation of the thermal frames and to compare the usability of the acquired thermal information under different operating conditions. Since raw radiometric matrices were not available, all image metrics were calculated from exported thermal images or grayscale-converted thermal frames.

Before analysis, each selected thermal frame was converted into an 8-bit grayscale image. The grayscale intensity values were then used to calculate global and region-of-interest-based indicators. These metrics were not used to estimate absolute thermal accuracy, but to compare relative image information content, contrast, and stability between different acquisition conditions.

The entropy of each thermal frame was calculated as:

$$H = -\sum_{i-1}^{L-1} p_i \log_2(p_i), \quad (3)$$

where H is the image entropy, L is the number of grayscale intensity levels, and p_i is the probability of occurrence of intensity level i. Higher entropy indicates a broader distribution of image intensities and greater visual information content, while lower entropy indicates a more uniform or poorly contrasted image.

The mean grayscale intensity of a selected region of interest was calculated as:

$$\mu_{ROI} = \frac{1}{N}\sum_{j=1}^{N} I_j. \quad (4)$$

The standard deviation within the ROI was calculated as:

$$\sigma_{ROI} = \sqrt{\frac{1}{N-1}\sum_{j=1}^{N}(I_j - \mu_{ROI})^2}. \quad (5)$$

The coefficient of variation was used as a normalized measure of intensity variation within the ROI:

$$CV = \frac{\mu_{ROI}}{\sigma_{ROI}} 100. \quad (6)$$

The signal-to-noise ratio was estimated as:

$$SNR = \frac{\mu_{ROI}}{\sigma_{ROI}}. \quad (7)$$

For target visibility assessment, the contrast between a selected target region and a background region was calculated as:

$$C_{T-B} = \left|\mu_{target} - \mu_{backgraund}\right|. \quad (8)$$

When temperature values were available from the thermal camera software or application display, the target-to-background temperature difference was calculated as:

$$\Delta T = T_{target} - T_{backgraund}. \quad (9)$$

For global frame uniformity, the following uniformity index was used:

$$UI = 1 - \frac{\sigma_{global}}{I_{max} - I_{min}}. \quad (10)$$

The selected metrics are summarized in Table 3.

Table 3. Image-based thermal frame quality indicators used in the study.

Metric	Formula	Interpretation
Entropy	$H = -\sum_{j-1}^{L-1} p_i \log_2(p_i)$	Relative image information content
Mean intensity	$\mu_{ROI} = \frac{1}{N}\sum_{j=1}^{N} I_j$	Average grayscale level in the ROI
Standard deviation	$\sigma_{ROI} = \sqrt{\frac{1}{N-1}\sum_{j=1}^{N}(I_j - \mu_{ROI})^2}$	Intensity variation within the ROI
Coefficient of variation	$CV = \frac{\mu_{ROI}}{\sigma_{ROI}} 100$	Normalized ROI variation

 doi:10.20944/preprints202606.0679.v1

Signal-to-noise ratio	$SNR = \frac{\mu_{ROI}}{\sigma_{ROI}}$	Relative image-based signal stability
Target-background contrast	$C_{T-B} = \lvert\mu_{target} - \mu_{backgraund}\rvert$	Selected target region and a background region
Temperature difference	$\Delta T = T_{target} - T_{backgraund}$	Comparative thermal contrast
Uniformity index	$UI = 1 - \frac{\sigma_{global}}{I_{max} - I_{min}})$	Relative global frame uniformity

2.9. Flight Endurance and Battery Drain

Flight endurance was evaluated under no-payload and payload conditions. The reduction in flight endurance was calculated as:

$$\boldsymbol{R_t = \frac{t_{baseline} - t_{payload}}{t_{baseline}} . 100} \quad (11)$$

where $\boldsymbol{R_t}$ is the relative endurance reduction, $\boldsymbol{t_{baseline}}$ is the no-payload flight time, and $\boldsymbol{t_{payload}}$ is the payload flight time.

For the near-ground hover case:

$$\boldsymbol{t_{baseline} = 25\ min}$$

$$\boldsymbol{t_{payload} = 14.67\ min}$$

then:

$$\boldsymbol{R_t = \frac{25 - 14.67}{25} . 100 \approx 41.3\%}$$

For the intensive flight profile including ascent to 120 m:

$$\boldsymbol{t_{payload,intensive} = 13\ min}$$

$$\boldsymbol{R_t = \frac{25 - 13}{25} . 100 \approx 48\%}$$

The battery drain rate was calculated as:

$$\boldsymbol{BDR = \frac{B_{start} - B_{end}}{t}} \quad (12)$$

where $\boldsymbol{BDR}$ is the battery drain rate, $\boldsymbol{B_{start}}$ is the battery level at the beginning of the flight, $\boldsymbol{B_{end}}$ is the battery level at the end of the flight, and $\boldsymbol{t}$ is the flight duration.

2.10. Motor Thermal Loading

Motor thermal loading was evaluated using UTi260T thermal images acquired after selected no-payload and payload flights. The motor temperature increase was calculated as:

$$\boldsymbol{\Delta T_{motor} = T_{motor,payload} - T_{motor,no-payload}} \quad (13)$$

When ambient or background temperature was available, the normalized motor temperature rise was calculated as:

$$\boldsymbol{\Delta T_{motor} = T_{motor} - T_{ambinet}} \quad (14)$$

The maximum motor temperature was defined as:

$$\boldsymbol{T_{max} = \max (T_{M1}, T_{M2}, T_{M3}. T_{M4})} \quad (15)$$

Motor thermal asymmetry was defined as:

 doi:10.20944/preprints202606.0679.v1

$$TA = T_{max} - T_{min} \quad (16)$$

where T_{max} and T_{min} are the maximum and minimum motor-region temperatures after flight. This parameter was used to evaluate whether the payload caused uneven propulsion loading.

2.11. Exploratory Correlation Analysis

An exploratory correlation analysis was planned to evaluate relationships between system configuration, flight conditions, thermal loading, and image usability. The main relationships considered were:

- payload condition vs. motor temperature increase;
- payload condition vs. flight endurance;
- payload condition vs. battery drain rate;
- illumination condition vs. screen readability;
- altitude vs. image usability;
- wind/oscillation vs. usable frames;
- motor thermal asymmetry vs. warning occurrence;
- flight stability vs. thermal visibility.

For numerical variables, the Spearman correlation coefficient was selected as the preferred method because of the limited dataset size and possible non-linear relationships:

$$\rho S_{pearman} \quad (17)$$

The analysis was treated as exploratory rather than confirmatory.

3. Results

3.1. Feasibility of the Low-Cost UAV Thermal Configuration

The first experimental result was the successful operation of the UTi260M smartphone-connected thermal camera with the lightweight Servo King900 smartphone. This combination formed a functional thermal display and recording module with a mass below 100 g. The complete UAV-payload configuration had a measured mass of approximately 340 g and was successfully lifted by the DJI Mini 4K platform.

This confirmed the basic feasibility of the proposed low-cost indirect UAV thermal sensing workflow. The system was able to acquire a primary thermal stream through the smartphone application and simultaneously allow the UAV onboard RGB camera to record the smartphone-displayed thermal image during flight.

Using Equations (1) and (2), the effective added payload was calculated as 91 g, corresponding to a payload-to-UAV mass ratio of 36.5%. These calculated values were used to interpret the subsequent endurance, motor-loading, and stability results.

3.2. Payload Effect on Flight Endurance

The no-payload UAV baseline flight was completed without abnormal behavior and achieved approximately 25 min of near-ground hover endurance. With the suspended Servo King900 + UTi260M payload, the near-ground hover endurance decreased to approximately 14 min 40 s. Under a more intensive flight profile involving active stabilization and ascent to 120 m, the payload endurance decreased further to approximately 13 min. The measured endurance values and relative reductions are summarized in Table 4.

The relative endurance reductions reported in Table 4 were calculated using Equation (11), with the no-payload hover endurance used as the baseline reference.

 doi:10.20944/preprints202606.0679.v1

Table 4. Flight endurance under no-payload and payload conditions.

Configuration	Flight mode	Approximate endurance	Relative reduction
No payload	near-ground hover	~25 min	—
Payload	near-ground hover	~14 min 40 s	~41.3%
Payload	intensive profile with ascent to 120 m	~13 min	~48%

According to Equation (11), the payload-hover endurance reduction was approximately 41.3%, while the intensive payload-flight profile resulted in an endurance reduction of approximately 48.0%.

The results show that the payload configuration significantly reduced flight endurance. The 14 min 40 s value should be interpreted as a near-ground hover reference rather than a full mission endurance value. More demanding flight profiles involving horizontal displacement, ascent, descent, wind compensation, and payload oscillation damping further increased propulsion demand and reduced usable flight duration.

3.3. Payload Effect on Motor Thermal Loading

Thermal inspection showed a substantial increase in motor temperature under payload conditions. In representative tests, the no-payload condition showed a maximum observed motor-region temperature of approximately 23.5 °C, while the payload condition showed values up to approximately 42.2 °C. The difference reached approximately 18.7–20 °C, indicating a strong payload-induced increase in propulsion thermal load.

Table 5. Representative motor thermal loading comparison under no-payload and payload conditions.

Condition	Representative maximum motor-region temperature	Observation
No payload	~23.5 °C	Normal behavior, no warnings
Payload	~42.2 °C	Increased motor loading
Difference	~18.7–20 °C	Payload-induced thermal penalty

The maximum motor-region temperatures were interpreted according to Equation (15), while the comparison between loaded and unloaded cases was used to assess the payload-induced thermal penalty.

Baseline flights without payload were completed without instability, propulsion warnings, or abnormal thermal loading. In contrast, the suspended payload configuration produced increased motor temperatures and occasional warnings. This indicates that the observed limitations were payload-induced rather than caused by a defective UAV platform.

3.4. Influence of Payload Orientation and Center-of-Gravity Offset

Repeated tests showed that payload orientation was a critical parameter. A slight forward inclination of the smartphone-thermal camera module toward the front motors caused increased thermal loading and persistent warning messages during flight. This confirmed that the system is highly sensitive not only to payload mass, but also to payload alignment and center-of-gravity offset.

The effect can be explained by the moment generated by the suspended load. When the center of mass of the module is shifted forward, the propulsion system must continuously compensate for the resulting moment. This leads to asymmetric motor loading, increased heating, and reduced operational robustness.

3.5. Influence of Illumination and Display Brightness

Daylight operation was limited by display glare and reflections. Under direct sunlight, the smartphone-displayed thermal stream was more difficult to read from the UAV RGB recording. Nighttime and low-glare conditions provided substantially better display readability.

 doi:10.20944/preprints202606.0679.v1

In dark conditions, reducing the smartphone display brightness to approximately 50% improved the balance between visibility and overexposure. Maximum brightness was not always optimal during nighttime operation because it could overexpose parts of the smartphone display in the UAV RGB recording.

Representative frames illustrating the influence of illumination and display brightness are shown in Figure 4. During daylight operation, the smartphone-displayed thermal stream was difficult to interpret from the UAV RGB recording because of ambient illumination, reflections, and reduced display contrast. During nighttime operation, display readability improved; however, excessive smartphone brightness caused partial overexposure in the UAV RGB recording. Reducing the smartphone brightness improved the balance between display visibility and overexposure. The direct UTi260M thermal recording was used as the primary reference to verify the thermal content observed indirectly by the UAV camera.

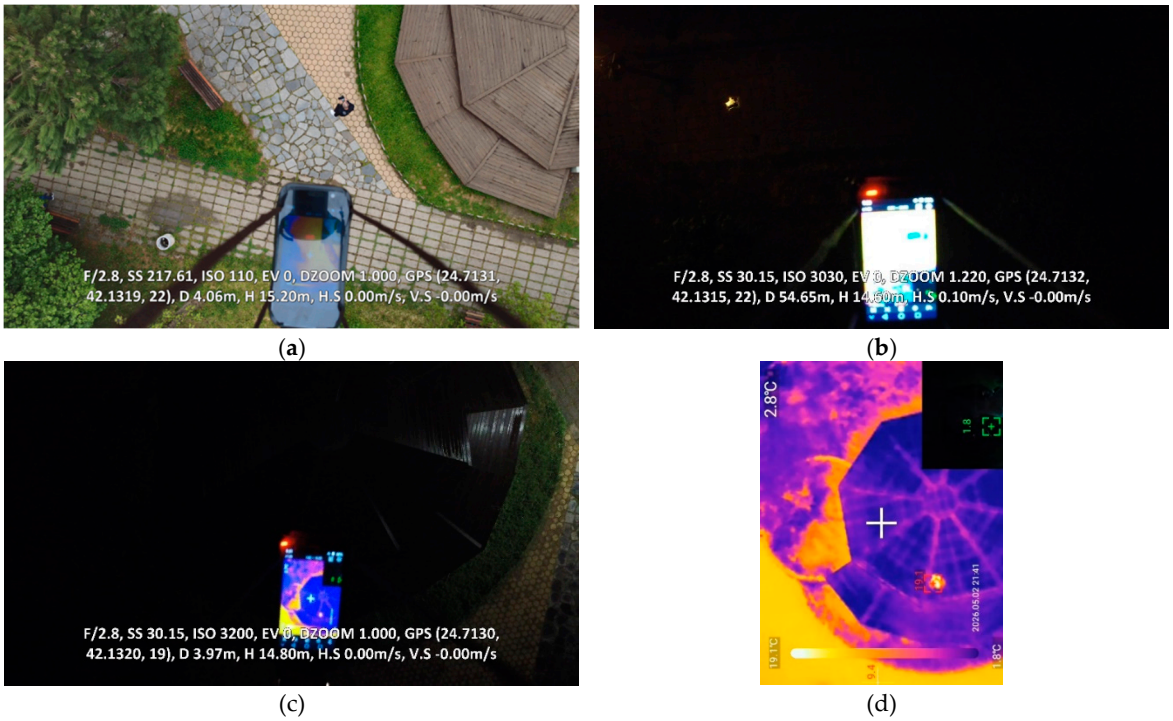

Figure 4. Influence of illumination and smartphone display brightness on indirect UAV thermal visualization: (a) daylight UAV RGB recording, where the smartphone-displayed thermal stream is poorly readable due to ambient illumination and reflections; (b) nighttime UAV RGB recording with high display brightness, resulting in partial overexposure of the display; (c) nighttime UAV RGB recording with reduced display brightness, showing improved readability of the thermal stream despite the suspended payload configuration; (d) direct thermal frame recorded by the Servo King900 smartphone with the UTi260M thermal camera, used as the primary thermal reference for cross-checking the UAV-recorded display frames.

The results indicate that illumination primarily affected image usability rather than flight endurance. Nighttime operation improved the visibility of the displayed thermal stream, but did not significantly reduce the energy penalty caused by the payload.

3.6. Altitude Range and Thermal Target Visibility

Nighttime tests showed that the smartphone-displayed thermal stream remained visible to the UAV RGB camera at several operating heights. Usable thermal visualization was observed at approximately 5–7 m, 10–15 m, 20 m, and up to approximately 24–25 m. The most practical image usability was observed in the 10–20 m range. At higher altitudes, the smartphone display remained visible but became smaller and more difficult to interpret. The observed image usability at different operating heights is summarized in Table 6.

 doi:10.20944/preprints202606.0679.v1

Table 6. Observed image usability by operating height.

Operating height	Observed image usability	Interpretation
5–7 m	good	low-altitude stabilization range
10–15 m	very good	most practical imaging window
20 m	good	thermal objects detectable
24–25 m	limited to usable	upper useful range for display readability
120 m	boundary/stress test	not recommended as normal operating mode

3.7. Stepwise Thermal Screening Protocol

Because the payload reduced endurance and increased motor thermal loading, the system is more suitable for short, sector-based screening than for continuous large-area surveys. A practical operating protocol consists of short flights to a selected sector, brief thermal observation, return before critical battery depletion, battery replacement, short motor cooling, system reset, and deployment over the next sector. The recommended stepwise thermal screening protocol is summarized in Table 7.

Table 7. Recommended stepwise thermal screening protocol.

Step	Purpose
Take-off and stabilization	Allow payload oscillation to settle
Short transit to sector	Avoid high-speed flight and excessive oscillation
Thermal observation	Record thermal stream and UAV display capture
Return with reserve	Prevent critical battery depletion
Controlled landing	Avoid abrupt motion and payload swing
Battery replacement	Restore endurance for next sector
Short motor cooling	Reduce accumulated propulsion heat
Next sector	Repeat the procedure over the next area

3.8. Dual-Channel Verification of Thermal Observations

Representative qualitative comparisons between the direct UTi260M thermal output and the UAV-recorded smartphone display are presented in Figure 5. The direct thermal frames provide clearer thermal boundaries and hotspot contrast, whereas the UAV RGB frames show the same thermal information indirectly through the smartphone display. Although the suspended smartphone module exhibited visible oscillation during flight, the thermal content remained visually distinguishable in several nighttime flight segments.

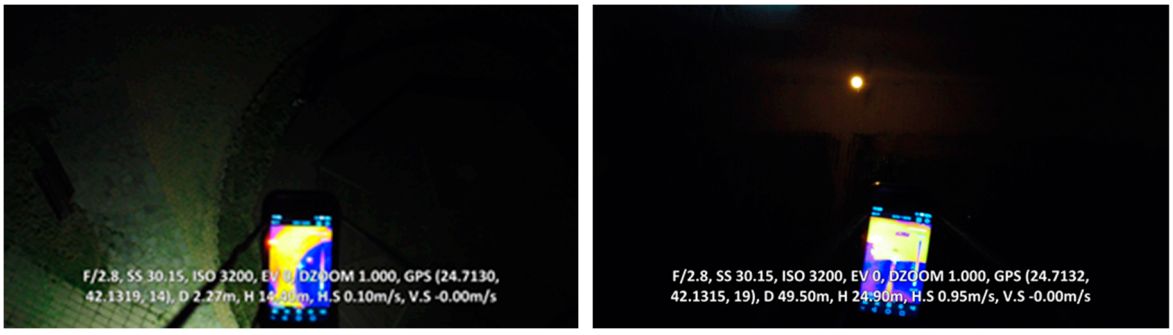

(a) (b)

 doi:10.20944/preprints202606.0679.v1

(c) (d)

Figure 5. Representative dual-channel comparison between direct thermal-camera output and UAV-recorded smartphone display: (a,c) direct thermal frames recorded by the Servo King900 smartphone with the UTi260M thermal camera; (b,d) corresponding or approximately corresponding UAV RGB frames showing the smartphone-displayed thermal stream during flight. The comparison demonstrates that the direct thermal stream provides clearer thermal information, while the UAV-recorded display remains usable for preliminary monitoring despite payload oscillation, reduced sharpness, display-related effects, and indirect optical acquisition.

3.9. Thermal Loading of UAV Motors under Loaded and Unloaded Conditions

To evaluate the effect of payload on motor thermal loading, thermal measurements were performed immediately after representative flights under loaded and unloaded conditions. Figure 6 compares the post-flight motor temperature distributions for both cases. Under loaded operation, the recorded temperatures were substantially higher and more spatially non-uniform, indicating increased motor loading. In contrast, the unloaded configuration showed lower and more balanced temperatures across the four motors.

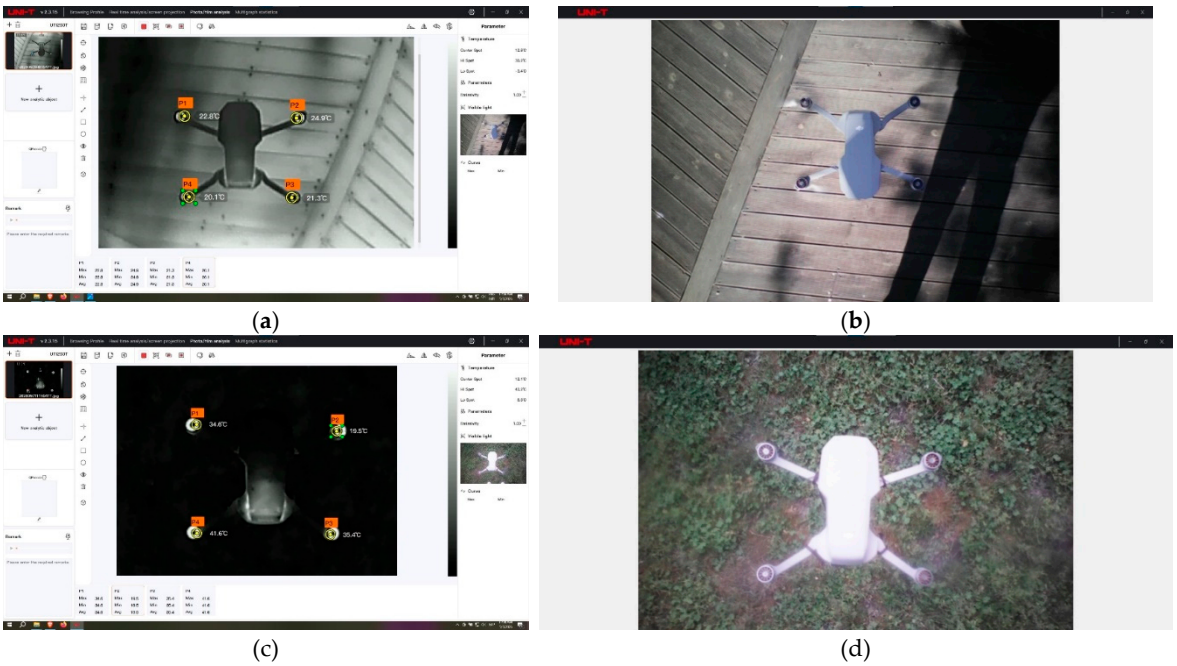

(**a**) (**b**)

(c) (d)

Figure 6. Comparison of the UAV motor thermal response under loaded and unloaded operating conditions: (a) visible-light reference image of the UAV after flight with payload; (b) thermal analysis of the UAV after flight with payload, showing higher motor temperatures and non-uniform thermal distribution; (c) visible-light reference image of the UAV after flight without payload; (d) thermal analysis of the UAV after flight without payload, showing lower and more uniform motor temperatures. Measurement points P1–P4 correspond to the four motor locations used for comparative thermal assessment. The point-based post-flight motor temperatures are summarized in Table 8.

 doi:10.20944/preprints202606.0679.v1

The point-based values extracted from the four motor regions were further used to calculate the maximum motor temperature and motor thermal asymmetry according to Equations (15) and (16).

Table 8. Post-flight motor temperatures with and without payload.

Motor	With payload (°C)	Without payload (°C)	Difference (°C)
P1	34.6	22.8	11.8
P2	19.5	24.9	-5.4
P3	35.4	21.3	14.1
P4	41.6	20.1	21.5

Using Equation (16), the motor thermal asymmetry increased from 4.8 °C under no-payload operation to 22.1 °C under payload operation. This increase supports the interpretation that the suspended payload caused non-uniform propulsion loading.

The thermal distribution was not perfectly symmetric, which is consistent with the off-center suspended payload, airflow interaction, and the non-rigid mounting configuration.

3.10. Payload-Induced Propeller Warning and Operational Failure Mode

During payload flights, the UAV occasionally displayed a "Propeller Error" warning, as shown in Figure 7. The warning was not observed during the no-payload baseline flights. The warning occurrence was associated with payload operation, especially when the suspended smartphone–thermal camera module was not ideally centered or was slightly inclined toward the front motors.

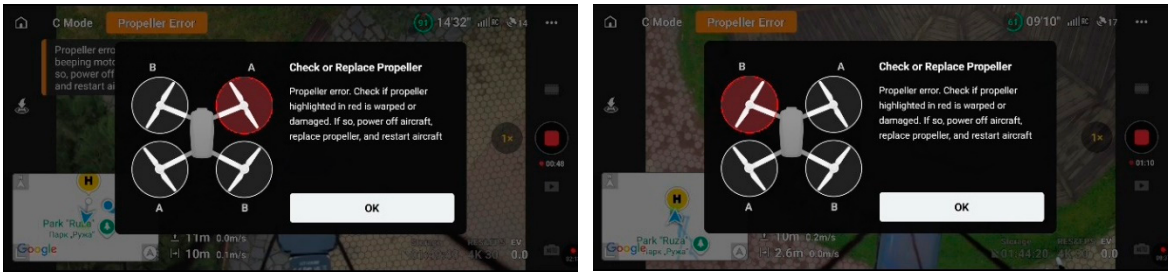

(**a**) (**b**)

Figure 7. Operational warnings observed during payload flights: (a,b) representative "Propeller Error" warnings associated with payload operation, center-of-gravity sensitivity, and increased propulsion loading; (c) "Critical low battery" warning during nighttime payload operation, showing the reduced endurance margin and the need for conservative mission planning.

3.11. Exploratory Operational Relationship Analysis

To summarize the main operational relationships observed during the experiments, selected descriptive plots were prepared from the measured endurance, motor-temperature, motor-asymmetry, and image-usability data. Because of the limited number of repeated trials, these plots were interpreted as exploratory operational relationships rather than statistically confirmatory correlations. The resulting exploratory operational plots are shown in Figure 8.

The Spearman-based approach defined in Equation (17) was therefore used only as an exploratory ranking concept, while the graphical results in Figure 8 were interpreted descriptively because several variable pairs contained only a small number of valid observations.

 doi:10.20944/preprints202606.0679.v1

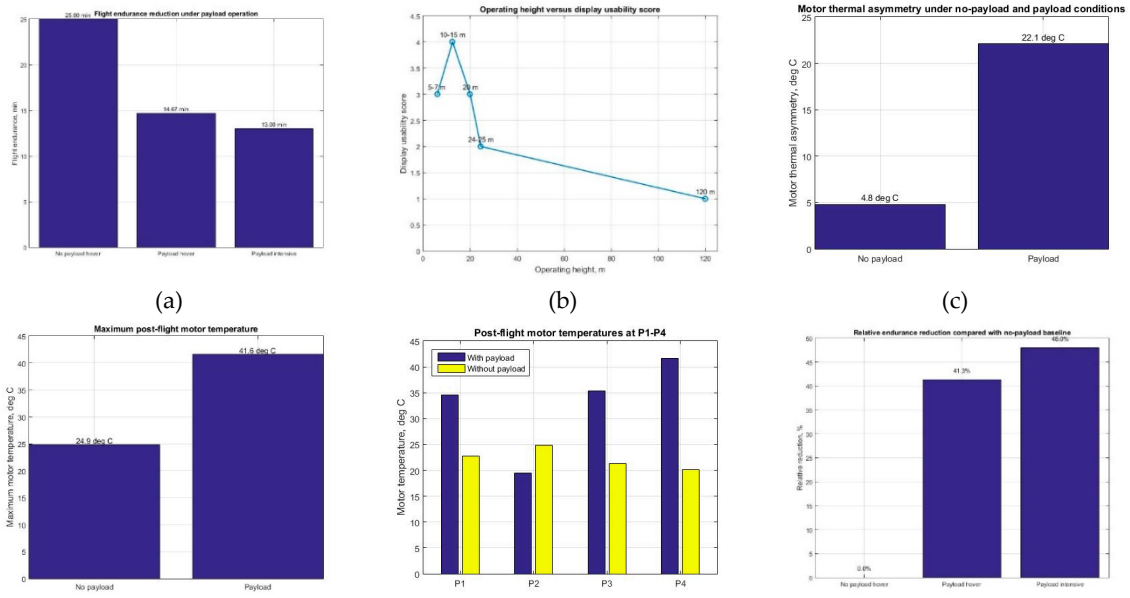

Figure 8. Exploratory operational relationships of the proposed UAV thermal sensing workflow: (a) flight endurance reduction under no-payload, payload-hover, and intensive payload-flight conditions; (b) post-flight motor temperatures at P1–P4 under loaded and unloaded conditions; (c) motor thermal asymmetry under no-payload and payload operation; (d) relationship between operating height and display usability score. The plots summarize the main observed tendencies: payload operation reduced endurance, increased motor thermal asymmetry, and produced higher non-uniform motor temperatures, while the best display usability was observed in the 10–20 m operating range.

4. Discussion

4.1. Feasibility and Cost-Constrained Design

The proposed configuration demonstrates that a functional low-cost UAV thermal sensing workflow can be achieved using a sub-250 g consumer drone, a lightweight smartphone, and a smartphone-connected thermal camera. The core airborne system cost was approximately 425 EUR, and the complete experimental setup including the auxiliary Armor 27T smartphone was approximately 725 EUR. This is substantially lower than dedicated professional thermal UAV platforms. However, the system should be interpreted as a low-cost preliminary screening workflow rather than as a replacement for professional radiometric thermal UAV systems.

4.2. Payload Penalty and Propulsion Stress

Although the payload mass was below 100 g, its relative contribution to the sub-250 g UAV platform was high. The effective payload ratio of approximately 36.5% resulted in measurable operational penalties: endurance reduction, increased motor temperature, and propulsion warnings under unfavorable payload alignment. These findings demonstrate that even a lightweight smartphone-based thermal module can significantly reduce the energy and propulsion margins of a small consumer UAV.

4.3. Importance of Payload Alignment, Suspension, and Rotor Downwash

The tests showed that payload geometry and alignment were critical. A slight inclination of the module toward the front motors increased motor heating and produced persistent warnings. The cord-based suspension minimized mass but introduced pendulum-like oscillation. In addition, the smartphone body was directly exposed to rotor downwash, which induced additional motion and reduced the stability of the displayed thermal image recorded by the UAV camera. These effects

 doi:10.20944/preprints202606.0679.v1

explain why a rigid lightweight mount would likely improve image stability, although its added mass could further increase propulsion loading on the selected UAV platform.

4.4. Why Nighttime Conditions Were Most Effective

The best image usability was observed in dark or low-glare conditions. Nighttime operation reduced display reflections and improved the ability of the UAV RGB camera to record the smartphone-displayed thermal stream. In addition, low ambient temperature can increase thermal target contrast because warm objects are more clearly separated from a colder background. This makes nighttime and low-ambient-temperature operation particularly suitable for preliminary localization of thermally contrasting objects such as humans, animals, warm mechanical components, engines, or localized heat sources.

4.5. Operational Window and Practical Use

The system is not suitable for long-range or large-area continuous surveys. Higher-capacity batteries would increase total mass and could further increase motor thermal loading. High-speed flight is also not recommended because the suspended payload becomes more prone to oscillation, reducing image usability. Therefore, the system is more appropriate for short-duration, stepwise thermal screening of selected areas under calm and low-glare conditions. The main experimental observations and their operational implications are summarized in Table 9.

Table 9. Main findings and operational implications.

Observation	Operational implication
System flies with payload	Concept is feasible
Flight endurance reduced from 25 min to 14 min 40 s / 13 min	Short missions only
Motor temperature increases by up to approximately 20 °C	Payload increases propulsion stress
Warnings appear only with payload	Limitations are payload-induced
Nighttime improves display readability	Low-glare operation is preferred
10–20 m provides useful images	Practical altitude window
Forward payload tilt causes warnings	Payload alignment is critical
Wind and downwash induce oscillation	Calm conditions and stabilization are required
Rigid mount could improve imaging but adds mass	Mass-stability trade-off

4.6. Limitations

The system has several limitations. The UTi260M data were acquired through a smartphone application rather than as raw radiometric matrices. The UAV RGB recording represents an indirect display capture and is affected by focus, exposure, compression, screen brightness, and payload motion. The payload configuration strongly affects motor loading and endurance. The system is sensitive to wind, center-of-gravity offset, payload orientation, and propeller downwash. Therefore, the results should be interpreted as a feasibility and operational boundary assessment rather than as a validation of a professional radiometric UAV thermal platform.

5. Conclusions

This study demonstrated the feasibility of a low-cost indirect UAV thermal sensing workflow based on a DJI Mini 4K consumer drone, a Servo King900 lightweight smartphone, and a UTi260M smartphone-connected infrared camera. The key enabling factor was the successful operation of the UTi260M with a sub-100 g smartphone module. The complete UAV-payload configuration had a measured mass of approximately 340 g, corresponding to an effective payload ratio of approximately 36.5%.

 doi:10.20944/preprints202606.0679.v1

Payload operation reduced near-ground flight endurance from approximately 25 min to approximately 14 min 40 s, corresponding to an approximate 41.3% reduction. Under an intensive flight profile including ascent to 120 m, endurance decreased to approximately 13 min, corresponding to an approximate 48% reduction. Motor thermal loading increased substantially, with differences of up to approximately 20 °C between payload and no-payload operation. Warnings occurred only under payload conditions, indicating that the limitations were induced by the suspended thermal module rather than by the UAV platform itself.

The system performed best under dark or low-glare conditions, where the smartphone display was more readable by the UAV onboard camera. Thermal objects were detectable up to approximately 20 m under favorable conditions, with the best practical image usability observed around 10–20 m. The proposed workflow is suitable for short-duration, stepwise preliminary thermal screening of selected areas, but not for professional radiometric inspection or large-area continuous surveys.

Future work should focus on a more capable UAV platform, a rigid lightweight mount, improved payload alignment, reduced exposure to rotor downwash, improved synchronization, and direct extraction of thermal data from the smartphone-connected camera.

Author Contributions: Conceptualization, Conceptualization, Y.S.; methodology, Y.S.; investigation, Y.S.; data curation, Y.S.; formal analysis, Y.S.; visualization, Y.S.; writing—original draft preparation, Y.S.; writing—review and editing, Y.S., A.T., P.M.; supervision, A.T.; resources, A.T., P.M.; project administration, Y.S. All authors have read and agreed to the published version of the manuscript.

Funding: This research was funded by the European Regional Development Fund within the OP "Research, Innovation and Digitalization Programme for Intelligent Transformation 2021-2027", Project No BG16RFPR002-1.014-0005 Center of competence "Smart Mechatronics, Eco- and Energy Saving Systems and Technologies".

Institutional Review Board Statement: Ethical review and approval were waived for this study due to its retrospective character and the fact that it only involved contactless collected data. The study did not have a medical purpose and therefore does not fall under the jurisdiction of the ethics committee.

Abbreviations

The following abbreviations are used in this manuscript:

UAV	Unmanned aerial vehicle
RGB	Red, green, blue
LWIR	Long-wave infrared
ROI	Region of interest
SRS	Screen Readability Score
FSS	Flight Stability Score
TVS	Thermal Visibility Score
OSI	Operational Suitability Index
BDR	Battery Drain Rate

References

1. Bohnett, E.; Lamichanne, B.R.; Chaudhary, S.; Pokhrel, K.; Dorman, G.; Flores, A.; Lewison, R.; Qiu, F.; Stow, D.; An, L. Thermal Infrared UAV Applications for Spatially Explicit Wildlife Occupancy Modeling. Land 2025, 14, 1461. https://doi.org/10.3390/land14071461
2. Yeom, S. Thermal Image Tracking for Search and Rescue Missions with a Drone. Drones 2024, 8, 53. https://doi.org/10.3390/drones8020053
3. Paciolla, F.; Popeo, G.; Farella, A.; Pascuzzi, S. Agronomic Information Extraction from UAV-Based Thermal Photogrammetry Using MATLAB. Remote Sens. 2025, 17, 2746. https://doi.org/10.3390/rs17152746
4. Pinel-Ramos, E.J.; Spaan, D.; Wich, S.; Aureli, F. Thermal Drones Aid to Uncover Nocturnal Subgrouping Patterns of a Diurnal Primate. Drones 2026, 10, 114. https://doi.org/10.3390/drones10020114

 doi:10.20944/preprints202606.0679.v1

5. Sam-Odusina, T.; Perkasa, P.; Chalmers, C.; Fergus, P.; Longmore, S.N.; Wich, S.A. Detection and Geolocation of Peat Fires Using Thermal Infrared Cameras on Drones. Drones 2025, 9, 459. https://doi.org/10.3390/drones9070459
6. Massey, L.; Foley, A.M.; Baumgardt, J.; DeYoung, R.W.; Perotto-Baldivieso, H.L. Pre-Programming Thermal Sensors Improves Detection During Drone-Based Nocturnal Wildlife Surveys in Warm Weather. Drones 2026, 10, 127. https://doi.org/10.3390/drones10020127
7. Larsen, H.L.; Møller-Lassesen, K.; Enevoldsen, E.M.E.; Madsen, S.B.; Obsen, M.T.; Povlsen, P.; Bruhn, D.; Pertoldi, C.; Pagh, S. Drone with Mounted Thermal Infrared Cameras for Monitoring Terrestrial Mammals. Drones 2023, 7, 680. https://doi.org/10.3390/drones7110680
8. Chang, B.; Hwang, B.; Lim, W.; Kim, H.; Kang, W.; Park, Y.-S.; Ko, D.W. Enhancing Wildlife Detection Using Thermal Imaging Drones: Designing the Flight Path. Drones 2025, 9, 52. https://doi.org/10.3390/drones9010052
9. Burke, C.; McWhirter, P.R.; Veitch-Michaelis, J.; McAree, O.; Pointon, H.A.G.; Wich, S.; Longmore, S. Requirements and Limitations of Thermal Drones for Effective Search and Rescue in Marine and Coastal Areas. Drones 2019, 3, 78. https://doi.org/10.3390/drones3040078
10. Henn, K.A.; Peduzzi, A. Surface Heat Monitoring with High-Resolution UAV Thermal Imaging: Assessing Accuracy and Applications in Urban Environments. Remote Sens. 2024, 16, 930. https://doi.org/10.3390/rs16050930
11. Rattanaamporn, S.; Perera, A.; Nguyen, A.; Ngo, T.B.; Chahl, J. Drone Imaging and Sensors for Situational Awareness in Hazardous Environments: A Systematic Review. J. Sens. Actuator Netw. 2025, 14, 98. https://doi.org/10.3390/jsan14050098
12. Bartlett, B.; Santos, M.; Dorian, T.; Moreno, M.; Trslic, P.; Dooly, G. Real-Time UAV Surveys with the Modular Detection and Targeting System: Balancing Wide-Area Coverage and High-Resolution Precision in Wildlife Monitoring. Remote Sens. 2025, 17, 879. https://doi.org/10.3390/rs17050879
13. Chen, R.; Li, D.; Gao, Z.; Kuai, Y.; Wang, C. Drone-Based Visible–Thermal Object Detection with Transformers and Prompt Tuning. Drones 2024, 8, 451. https://doi.org/10.3390/drones8090451
14. Kapil, R.; Castilla, G.; Marvasti-Zadeh, S.M.; Goodsman, D.; Erbilgin, N.; Ray, N. Orthomosaicking Thermal Drone Images of Forests via Simultaneously Acquired RGB Images. Remote Sens. 2023, 15, 2653. https://doi.org/10.3390/rs15102653
15. Pinel-Ramos, E.J.; Aureli, F.; Wich, S.; Longmore, S.; Spaan, D. Evaluating Thermal Infrared Drone Flight Parameters on Spider Monkey Detection in Tropical Forests. Sensors 2024, 24, 5659. https://doi.org/10.3390/s24175659
16. Tanda, G.; Balsi, M.; Fallavollita, P.; Chiarabini, V. A UAV-Based Thermal-Imaging Approach for the Monitoring of Urban Landfills. Inventions 2020, 5, 55. https://doi.org/10.3390/inventions5040055
17. Pérez-Álvarez, R.; Sedano-Cibrián, J.; de Luis-Ruiz, J.M.; Fernández-Maroto, G.; Pereda-García, R. Mining Exploration with UAV, Low-Cost Thermal Cameras and GIS Tools—Application to the Specific Case of the Complex Sulfides Hosted in Carbonates of Udías (Cantabria, Spain). Minerals 2022, 12, 140. https://doi.org/10.3390/min12020140
18. Thürkow, F.; Teucher, M.; Thürkow, D.; Mohri, M. Stone Detection on Agricultural Land Using Thermal Imagery from Unmanned Aerial Systems. AgriEngineering 2025, 7, 203. https://doi.org/10.3390/agriengineering7070203
19. Mirzabeigi, S.; Razkenari, R.; Crovella, P. A Review of the Potential of Drone-Based Approaches for Integrated Building Envelope Assessment. Buildings 2025, 15, 2230. https://doi.org/10.3390/buildings15132230
20. Henry, C.; Poudel, S.; Lee, S.-W.; Jeong, H. Automatic Detection System of Deteriorated PV Modules Using Drone with Thermal Camera. Appl. Sci. 2020, 10, 3802. https://doi.org/10.3390/app10113802
21. Jin, H.; Köppl, C.J.; Fischer, B.M.C.; Rojas-Conejo, J.; Johnson, M.S.; Morillas, L.; Lyon, S.W.; Durán-Quesada, A.M.; Suárez-Serrano, A.; Manzoni, S.; et al. Drone-Based Hyperspectral and Thermal Imagery for Quantifying Upland Rice Productivity and Water Use Efficiency after Biochar Application. Remote Sens. 2021, 13, 1866. https://doi.org/10.3390/rs13101866

 doi:10.20944/preprints202606.0679.v1

22. A. Tashev, and E. Dimitrov. Investigation of LPG influence on cylinder pressure of VW 1.9D diesel engine operating in dual-fuel mode. AIP Conf. Proc. vol. 3274, 060003, 2025. https://doi.org/10.1063/5.0258924.
23. P. Mitev "Development of a Training Station for the Orientation of Dice Parts with Machine Vision". Eng. Proc. 2024, vol. 70, no.1, https://doi.org/10.3390/engproc2024070057.
24. Mladenov, G.; Kuzmanov, N.; Hristov, V. Research on and Analysis of Brake Fluid Impact on Brake System Performance. Eng. Proc. 2025, 100, 27. https://doi.org/10.3390/engproc2025100027.
25. Ambarev, K.; Taneva, S. Thermal and Structural Analysis of Gasoline Engine Piston at Different Boost Pressures. Eng. Proc. 2025, 100, 38. https://doi.org/10.3390/engproc2025100038.
26. Radulov, A.; Dechev, M.; Matsankov, M. Investigation of the Efficiency of a Peltier Element. Eng. Proc. 2025, 100, 8. https://doi.org/10.3390/engproc2025100008.
27. Author 1, A.B. Title of Thesis. Level of Thesis, Degree-Granting University, Location of University, Date of Completion.
28. Title of Site. Available online: URL (accessed on Day Month Year).